

Electrical Pulsed Infrared Thermography and supervised learning for PV cells defects detection

Chiwu Bu^{a,*}, Tao Liu^a, Rui Li^a, Runhong Shen^a, Bo Zhao^a, Qingju Tang^b

^a School of Light Industry, Harbin University of Commerce, Harbin, 150028, PR China

^b School of Mechanical Engineering, Heilongjiang University of Science and Technology, Harbin, 150022, PR China



ARTICLE INFO

Keywords:

PV cells defects
Electrical pulsed infrared thermography
Supervised learning
Defects detection
SNR

ABSTRACT

As the most basic elements of photovoltaic (PV) module and power station, the defects in PV cells can affect the overall performance of the module and the operation status of the power station. Therefore, it is very important to carry out defects detection of PV cells. In this work, we have built an Electrical Pulsed Infrared Thermography (EPIT) experimental system to detect PV cells with different types of defects, such as broken gate, hidden crack, scratch and hot spot. Then, thermography sequence information of PV cells is captured by an infrared camera. Linear Discriminant Analysis (LDA) and Quadratic Discriminant Analysis (QDA), the two supervised learning (SL) algorithms, are used to process the thermography sequence and recognize the defects. In addition, the identification effect of the two algorithms is quantitatively evaluated by signal-to-noise ratio (SNR). The experiment results show that the EPIT method can realize the PV cells defects detection. Under different bias excitation, QDA algorithm is superior to LDA in SNR index, which can identify various defects of PV cells effectively.

1. Introduction

The recent growth in renewable power capacity has been mainly led by solar photovoltaic (PV) [1]. PV cells are important elements of module and power station, the generation efficiency of the module and operation status of the power station are affected by the qualities of cells [2]. During manufacturing and soldering, PV cells undergo thermo-mechanical stresses, which can lead to cell hidden cracking, broken gate, scratch defects and so on [3,4]. Therefore, the nondestructive testing (NDT) of PV cells defects is essential and important [5,6].

The detection methods of PV cells defects usually include electrical current-voltage (I-V) curves [7], electroluminescence (EL) [8], visual inspection [9] and so on. Infrared thermography (IRT) method is widely used because of its advantages of non-contact, large measurement area and good measurement effect [10]. IRT used for PV cells defects detection includes IULT (Infrared Ultrasound Lock-in Thermography) [11], ECT (Eddy Current Thermography) [12], DLIT (Dark Lock-in Thermography) [13,14] and ILIT (Illuminated Lock-in Thermography) [15]. However, facing with a variety of types of solar cell defects, these technologies cannot successfully detect defects such as hidden crack, scratch, and black core. Therefore, in this paper, EPIT (Electrical Pulsed

Infrared Thermography) is present here, the thermal contrast between the sound area and the defect area can be improved by pulsed bias voltage excitation, and the different types of defects can be recognized effectively.

For the existing various IRT methods, the detection of PV cells defects unable to meet the production requirements only by thermography, since the existing noises caused by electric excitation and emissivity variation of sample surface. Here, Linear Discriminant Analysis (LDA) and Quadratic Discriminant Analysis (QDA), the two supervised learning (SL) algorithms, are used to process the thermography sequence and improve the defects detection ability of EPIT.

This paper will investigate the application of EPIT as predictive program to identify the presence of various defects in PV cell samples, and apply two different post-processing algorithms, namely LDA and QDA to process the thermography sequence. This paper is organized as follows. First, heat dissipation and transport mechanisms in PV cell and infrared thermography set-up for PV cell defects testing are described in Section 2. Then, theory of LDA and QDA is presented in Section 3, and experimental study is finished in Section 4. Processing of thermography sequence by LDA and QDA is done in Section 5.

* Corresponding author.

E-mail address: buchiwu@126.com (C. Bu).

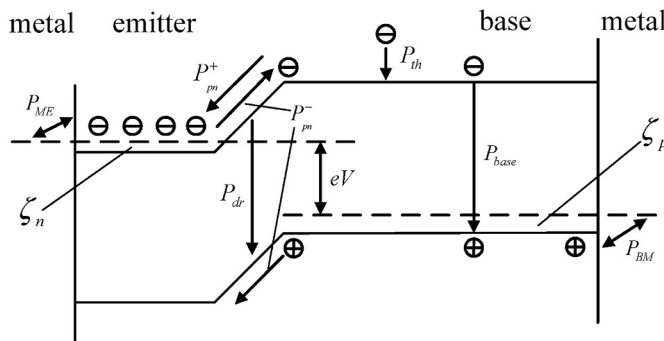


Fig. 1. Schematic diagram of heat dissipation mechanisms under forward bias.

2. Detection principle

2.1. Heat dissipation and transport mechanisms in PV cell

On the occasions of darkness and illumination, the electronic processes in PV cell are related to local heat generation or heat consumption (local cooling), the internal heat dissipation mechanisms of PV cell under forward bias are shown in Fig. 1. Where, P_{dr} is recombination in the depletion region, P_{base} is recombination of injected electrons in the base region or at the back surface, P_{th} is thermalization heat of absorbed photons, P_{ME} is Peltier heating or cooling at the metal-emitter contact, P_{pn}^- is Peltier cooling for carrier injection at the p-n junction, P_{pn}^+ is Peltier heating of photo-generated electrons crossing the barrier (it is the inverse process of P_{pn}^-), P_{BE} is Peltier heating or cooling at the base-metal contact, and P_J is Joule heating due to horizontal current flow in the emitter (not indicated in Fig. 1).

The above parameters are all associated with the layout, local defect distribution and the working point of the cell. Under the excitation of forward bias voltage V , the amounts of the different power densities are the follows [16].

$$P_{dr} = \frac{J_{dr}}{e} (E_g + \varepsilon_e^n + \varepsilon_h^p) \quad (1)$$

$$P_{base} = \frac{J_{diff}}{e} (E_g + \varepsilon_e^p - \varepsilon_h^p) \quad (2)$$

$$P_{ME} = -\frac{J_{ME}}{e} (\zeta_n + \varepsilon_e^n) \quad (3)$$

$$P_{pn}^- = -\frac{J_{diff}}{e} (E_g - \zeta_n - \zeta_p - eV + \varepsilon_e^p - \varepsilon_e^n) - \frac{J_{dr}}{e} (E_g - \zeta_n - \zeta_p - eV) \quad (4)$$

$$P_{BM} = -\frac{J_{BM}}{e} (\zeta_p + \varepsilon_h^p) \quad (5)$$

$$P_{th} = \frac{J_{ph}}{e} (hv - E_g - \varepsilon_e^p - \varepsilon_h^p) \quad (6)$$

$$P_{pn}^+ = \frac{J_{ph}}{e} (E_g - \zeta_n - \zeta_p - eV + \varepsilon_e^p - \varepsilon_e^n) \quad (7)$$

$$P_J = \rho_s J_s^2 \quad (8)$$

Where, J_{dr} is depletion region recombination current density (A/m^2), J_{diff} is diffusion (injection) current density (A/m^2), J_{ph} is photocurrent density (A/m^2), hv is photon energy, e is electron charge, E_g is band-gap energy, ε_e^n is the average kinetic energy of electrons entering the emitter, ε_e^p is the average kinetic energy of electrons entering the base, ε_h^p is the average kinetic energy of hole entering the base, J_{ME} is emitter contact current density (A/m^2), J_{BM} is base contact current density (A/m^2), ζ_n is difference between Fermi level in n material to the conduction-band edge, ζ_p is difference between Fermi level in p material to the valence-

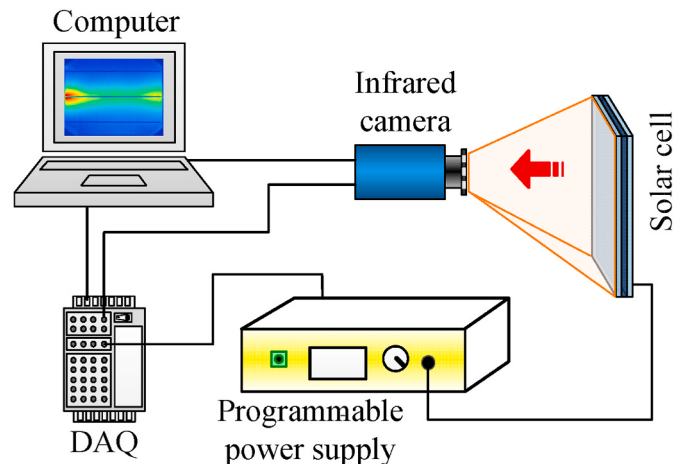


Fig. 2. Experimental setup of EPIT imaging system.

band edge, ρ_s is sheet resistance, and J_s^2 is sheet current density (A/m^2).

The equations (1)–(8) describe the heat dissipation and heat transport mechanisms in a PV cell, and P_{th} , P_{pn}^+ , and P_J should be neglected with forward bias on the occasions of darkness.

The actual PV cell is assumed to be homogeneous thermally thin. Therefore, for describing the dissipated power density in a PV cell in the dark, the net current density between metal and emitter J_{ME} and between metal and base J_{BM} both equal the dark current ($J_{ME} = J_{BM} = J_{diff} + J_{dr}$).

According to Eqs. (1)–(5), the total dissipated power of PV cell in the dark with the excitation of forward bias voltage V is as follow

$$P = P_{pn}^- + P_{dr} + P_{base} + P_{ME} + P_{BM} = V(J_{diff} + J_{dr}) \quad (9)$$

2.2. Experimental system

An EPIT imaging system has been set up and the schematic diagram is shown in Fig. 2. The PV cell is excited with a forward bias voltage produced by programmable power supply, the cell generates diffusion current and depletion region recombination current. Some defects in the PV cell will act as recombination centers by introducing different energy levels in the band gap, the heat dissipation and transport mechanisms of the PV cell will be affected, which shows that part of the current is converted into heat P and continues to accumulate, thus affecting the surface temperature distribution of the PV cell. We capture the surface temperature information of PV cell by infrared camera, and convert it into visual thermography sequence.

Under the excitation of forward bias voltage V , the three-dimensional heat conduction formula of PV cell can be expressed as [17].

$$\frac{\partial T}{\partial t} = \frac{k}{\rho C_p} \left(\frac{\partial^2 T}{\partial x^2} + \frac{\partial^2 T}{\partial y^2} + \frac{\partial^2 T}{\partial z^2} \right) + \frac{k}{\rho C_p} P(x, y, z, t) \quad (10)$$

Where, ρ , C_p and k represent the density (Kgm^{-3}), specific heat capacity ($\text{JKg}^{-1}\text{K}^{-1}$) and thermal conductivity ($\text{Wm}^{-1}\text{K}^{-1}$) of PV cell respectively.

The heat P diffuses in the PV cell with the form of thermal wave, and the temperature-change-rate of each point with time is related to its thermal diffusivity. The surface temperature of PV cell is considered to be equal to the internal diffusion temperature, and the cell surface temperature distribution with time can be calculated by

$$T_{surf}(t) = \frac{P}{\sqrt{\pi \rho C_p \lambda t}} \quad (11)$$

The temperature curves of point A and B in the sample are shown in

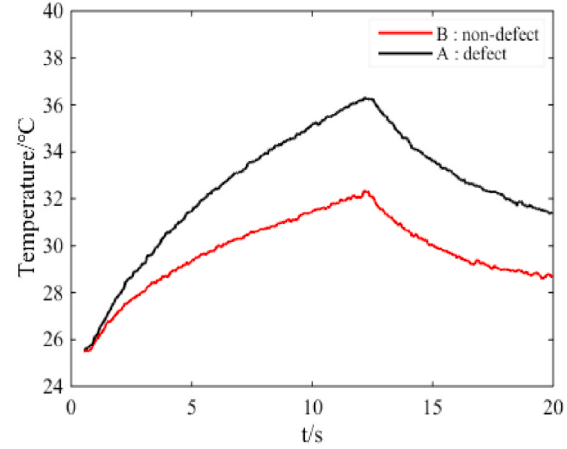
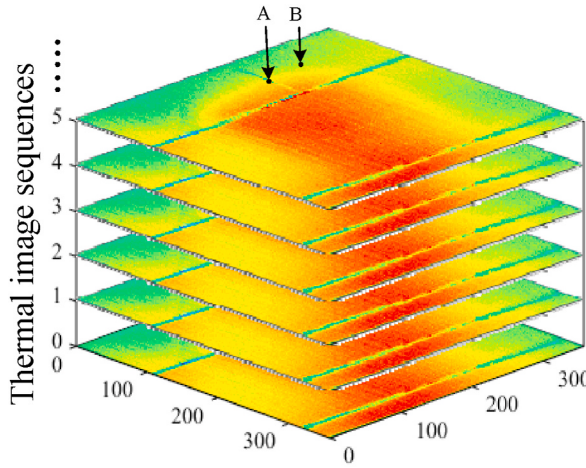


Fig. 3. Thermography sequence and temperature curves of selected points.

Fig. 3. Point A is randomly selected from the defect area, and point B is a random point close to point A from the sound area. It can be seen that there is an obvious temperature difference between point A and B, which indicates that the EPIT method can be adopted to detect the defects of PV cell.

3. Supervised learning (SL)

3.1. Background and target spectrum models

SL is used in target recognition and realized by means of a statistical hypothesis test. Whether a target feature is present in an image of the observed spectrum x , it can be defined by the following hypothesis:

$$\begin{aligned} G_0 &: x \sim N(\mu_b, R_b) \text{ target feature absent} \\ G_1 &: x \sim N(\mu_t, R_t) \text{ target feature present} \end{aligned}$$

Where, R_b is the covariance matrix of the background spectrum, R_t is the covariance matrix of the target spectrum, μ_t is the target spectrum, and μ_b is the background spectrum.

Background and target spectrum are modeled as random vectors with multivariate normal (or Gaussian), and the probability density functions is defined as [18].

$$P_i(x) = \frac{1}{(2\pi)^{m/2} \sqrt{|R|}} e^{-\frac{1}{2}(x-\mu_i)^T R^{-1} (x-\mu_i)} \quad (12)$$

Where, μ_i is the background or target spectrum average vector, R is the covariance matrix of the observed spectrum x , and $\|\cdot\|$ represents the matrix determinant.

For the purpose of theoretical analysis, Log-likelihood ratio (LLR) is modeled by the ratio of the conditional probability density functions with spectral variability and receiver noise are considered [18].

$$\delta(x) = \log \frac{P_1(x|G_1)}{P_0(x|G_0)} \stackrel{G_1}{\gtrless} \theta \quad (13)$$

Where, $P_1(x|G_1)$ is the probability density function without target background under G_1 condition; $P_0(x|G_0)$ is the probability density function of the target pixel under the condition of G_0 . If $\delta(x)$ is larger than the threshold θ , the hypothesis of “target feature present” is accepted, otherwise “target feature absent” is accepted.

3.2. Linear discriminant analysis (LDA) algorithm

LDA algorithm is one kind of SL algorithm, which can reduce the dimension of the images linearly. Compared with principal component



Fig. 4. Different defects of Polysilicon solar cells.

analysis (PCA) algorithm, LDA can use the spatial information of the sample data, avoid the over fitting phenomenon in the process of dimension reduction, and improve the recognition effect of defects in the images. If the covariance matrix of the target class and the background class is the same in the observation spectrum x , that is, $R_t = R_b = R$, LDA is used and its function is given by [19].

$$LDA = \left(-\frac{1}{2}\mu_t^T R^{-1} \mu_t + s^T R^{-1} \mu_t \right) - \left(-\frac{1}{2}\mu_b^T R^{-1} \mu_b + s^T R^{-1} \mu_b \right) \quad (14)$$

Where, s is the observed spectral vector of a given pixel, R^{-1} is the inverse covariance matrix of the observed spectrum x .

3.3. Quadratic discriminant analysis (QDA) algorithm

Similar to LDA, QDA algorithm is another SL algorithm. They have similar algorithm characteristics, the only difference is that if the target class and background class have different covariance matrices in the observed spectrum x , that is, $R_t \neq R_b$, QDA is used and its function is given by [19].

$$QDA = -\frac{1}{2} \log|R_t| - \frac{1}{2}(s - \mu_t)^T R_t^{-1} (s - \mu_t) \quad (15)$$

4. Experimental study

4.1. Samples preparation

Two pieces of polysilicon solar cell marked S1 and S2 (Fig. 4) are taken as the tested samples with broken gate, scratch, hidden crack and hot spot. The external sizes of both cells are 52mm × 52mm × 0.2 mm.

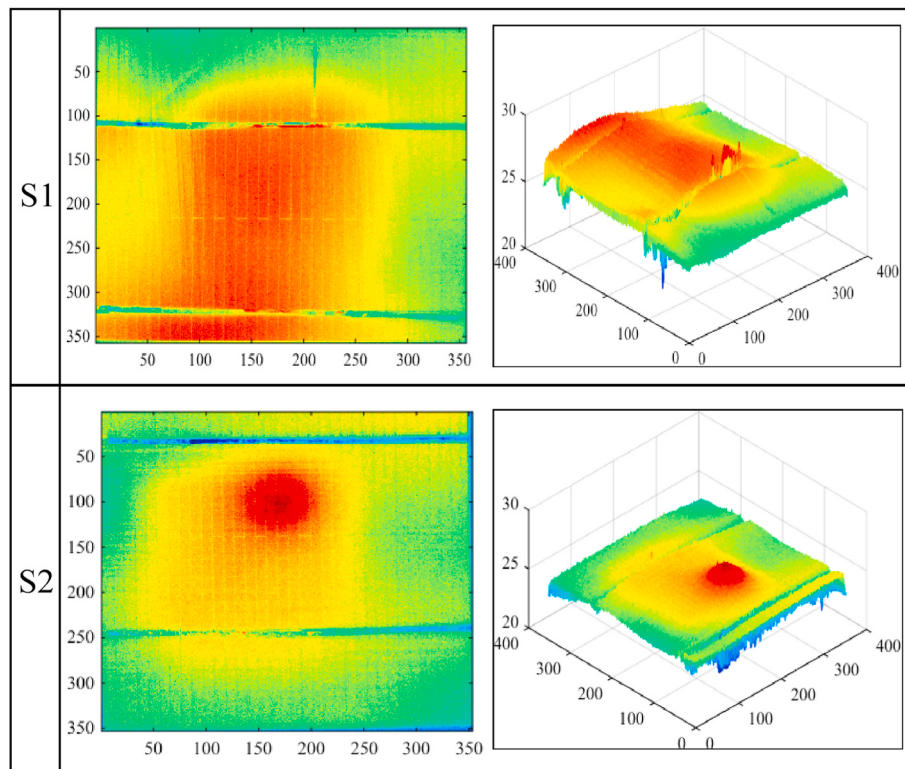


Fig. 5. The 50th frame from the original image of S1 and S2.

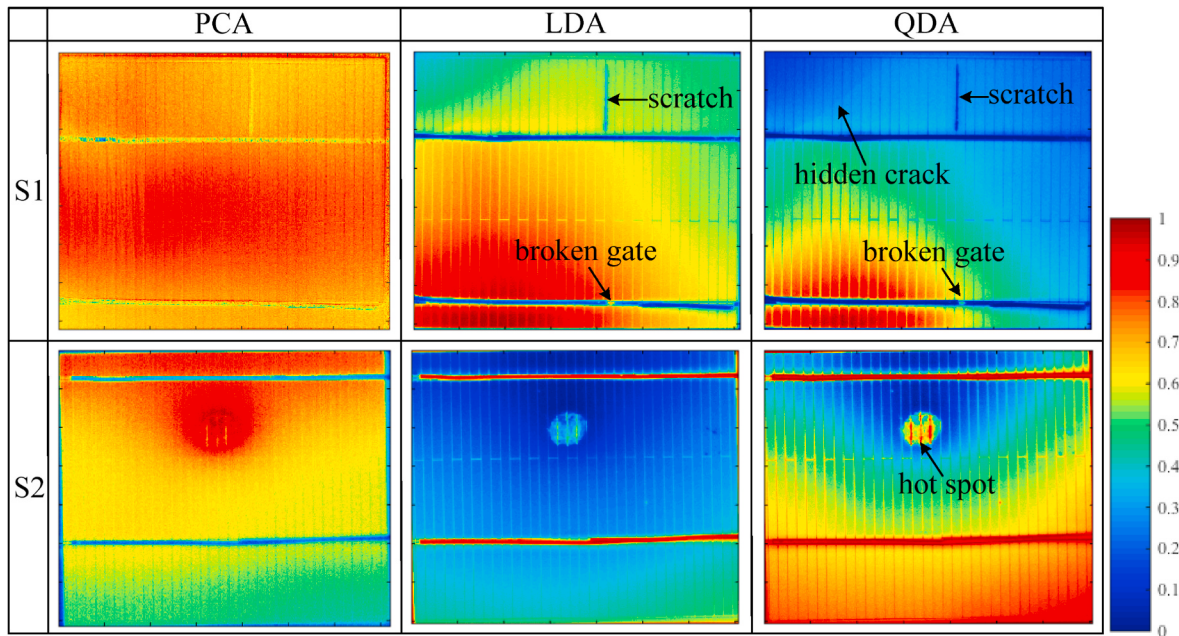


Fig. 6. Defects recognition results of S1 and S2 samples by PCA, LDA and QDA.

They are all low efficiency, in which the efficiency of S1 is 9.23% and that of S2 is 9.96%.

4.2. Parameter setting

The programmable power supply is modulated by a Data Acquisition (DAQ) card and provides pulse forward bias voltage as the electric excitation. An uncooled infrared camera (FLIR SC655, 640×480 , $7.5\text{--}14 \mu\text{m}$) is applied to capture the thermography sequence. With the

purpose of ensuring the synchronization of image acquisition and power excitation, the trigger signal for infrared camera image acquisition and the switch signal of programmable power supply are controlled by the DAQ card. The polysilicon PV cells (S1 and S2) are tested with the same testing parameters. Pulsed forward bias voltage is set as 1 V, excitation time is 12 s, sampling frequency is set as 20 Hz, and sampling period is set as 20 s. The thermography sequence of cell surface are collected and stored in the computer for subsequent processing and analysis.

The 50th frame from the original thermography sequence of S1 and

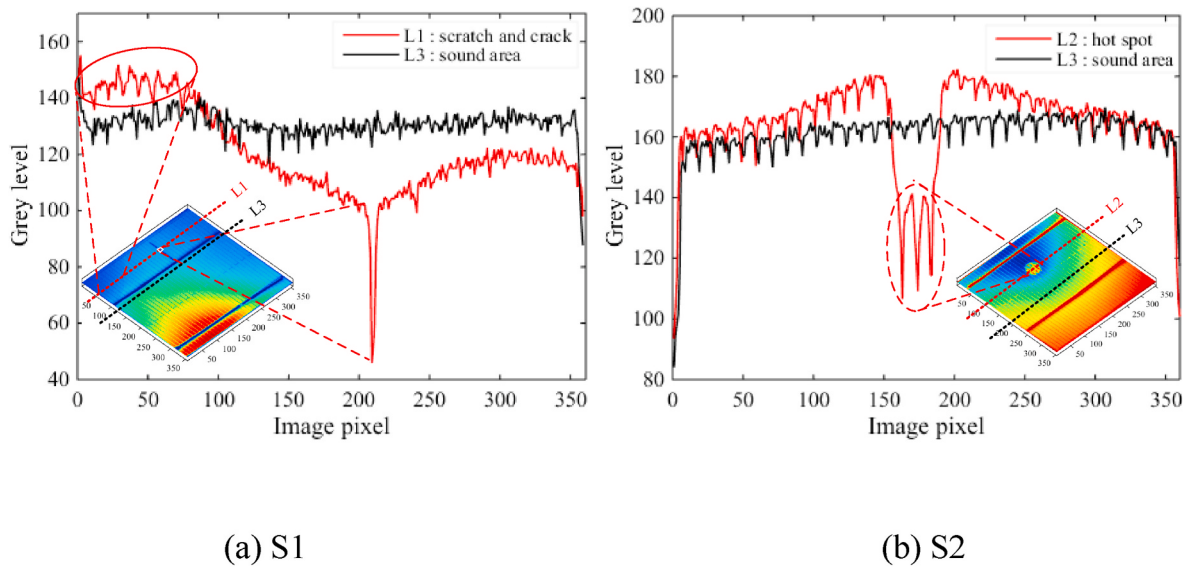


Fig. 7. Temperature information along the section lines.

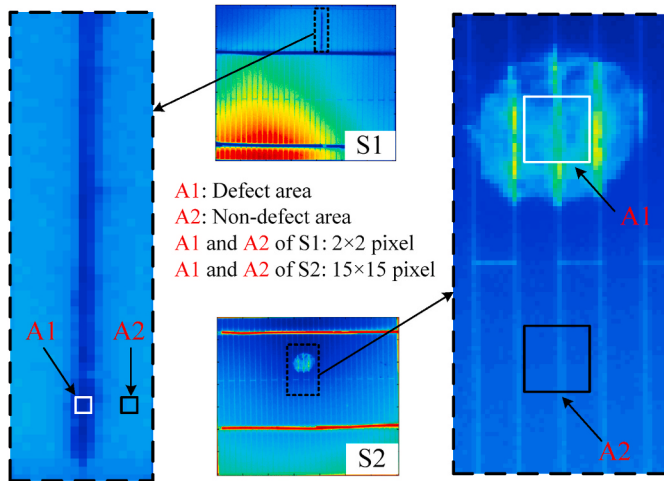


Fig. 8. The selection of the defect area and non-defect area.

S2 is shown in Fig. 5. A large number of noise interference signals exist in these two images, and it is difficult to recognize the defects information. Therefore, the thermography sequence needs to be processed to realize the defects recognition.

5. Results and discussions

5.1. Comparison of algorithm process results

The thermography sequence of S1 and S2 has been processed by PCA, LDA and QDA, and the results are shown in Fig. 6. In order to facilitate observation and comparison, the six images are linearly normalized. There is a hidden crack in the upper left corner of S1, which makes the

region separate from the main body, and there is an obvious temperature difference between them. Fig. 6 shows that QDA is better than PCA and LDA in the discrimination of hidden crack. Similarly, LDA and QDA also outperform PCA in identifying broken gate, scratch and hot spot. In addition, because different defects have different covariance matrices, QDA has the best processing effect in essence for the target class and background class with different covariance matrices. Therefore, QDA performs better than LDA in identifying different types of defects.

The above two images of S1 and S2 processed by QDA are selected to extract the information about hidden crack, scratch and hot spot. The section line L1 through hidden crack and scratch, L2 through hot spot and L3 through sound area are selected to show the corresponding temperature information in Fig. 7.

The position temperature of scratch (middle of L1) and hot spot (middle of L2) changes significantly, the position temperature of hidden crack (left end of L1) changes gently, and there is almost no difference in the temperature of sound area (L3).

5.2. Algorithm performance evaluation

The signal-to-noise ratio (SNR) of defect area is defined by [20].

$$\text{SNR} = \frac{|\overline{U}_{A1} - \overline{U}_{A2}|}{\sigma_{A2}} \quad (16)$$

Where, \bar{U}_{A1} is the mean value of defect area, \bar{U}_{A2} is the mean value of non-defect area and σ_{A2} is the standard deviation of non-defect area.

The selection of the defect area and non-defect area in the images are shown in Fig. 8. In S1, a block of 2×2 pixels in the scratch area is selected as the defect area A1, and the non-defect area A2 is selected in the sound area with the same pixels, which is located on the right side of A1 and separated by 18 pixels. In S2, a block of 15×15 pixels in the center of the hot spot area is selected as the defect area A1, the non-defect area A2 nearby A1 is selected in the sound area with the same pixels, which is located below A1 and separated by 52 pixels.

Table 1

The temperature of the cell S1 and S2.

Cell	1 V			1.5 V			2 V		
	T_{max} [°C]	$T_{healthy}$ [°C]	ΔT [°C]	T_{max} [°C]	$T_{healthy}$ [°C]	ΔT [°C]	T_{max} [°C]	$T_{healthy}$ [°C]	ΔT [°C]
S1	43.1	31.6	11.5	55.8	40.9	14.9	56.2	41.2	15
S2	47.2	40.8	6.4	52.6	44.2	8.4	53.1	44.7	8.4

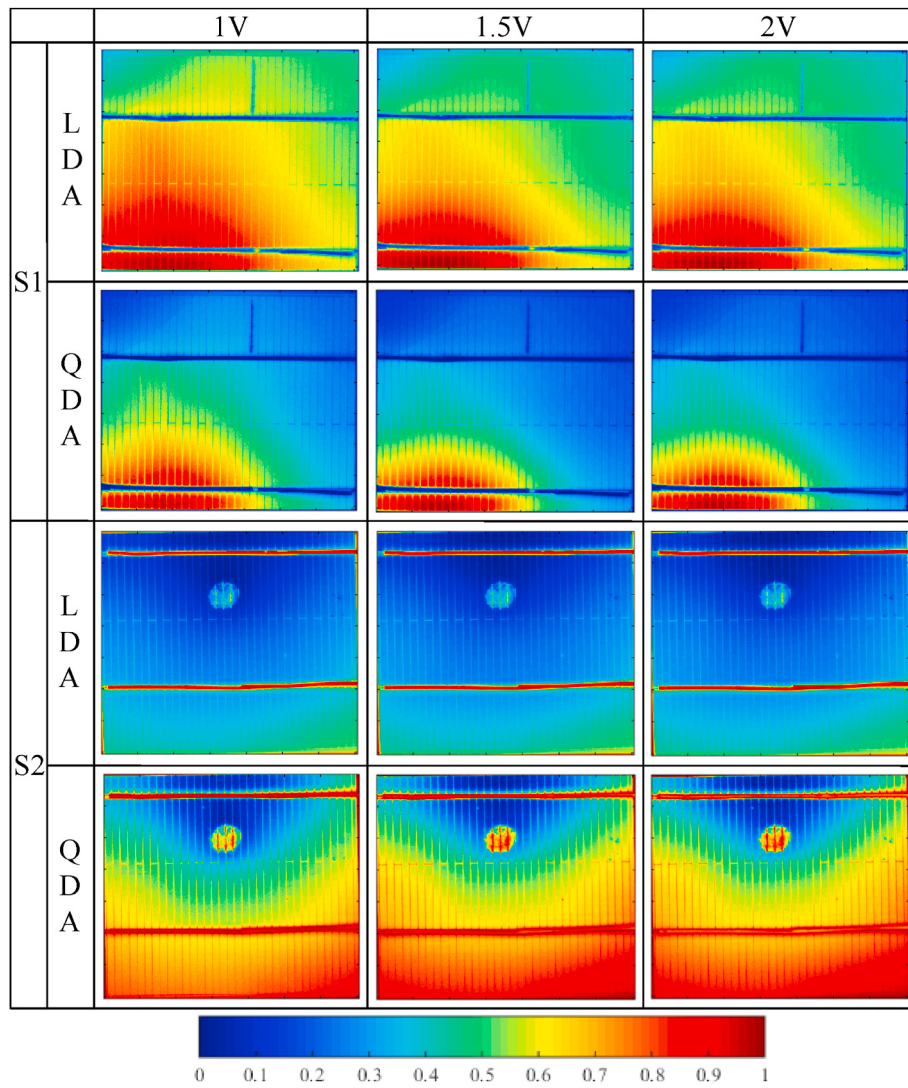


Fig. 9. The processing results of sample S1 and S2 by LDA and QDA.

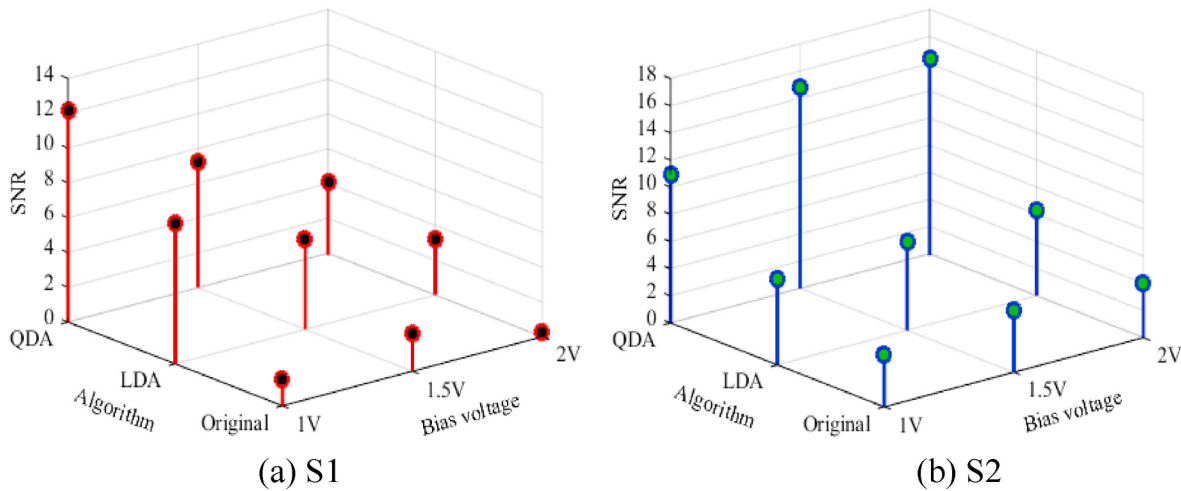


Fig. 10. The SNR of the processing results in Fig. 9.

It is the best working condition when the temperature of the PV cell is 25 °C; but when the temperature exceeds 60 °C, the life and efficiency of cell will be reduced seriously. In this condition, the detection effect of

cell defects can be improved by setting the bias voltage reasonably. We have tested S1 and S2 under different bias voltages. It can be found that the temperature rise of the cell is too slow when the voltage is less than 1

V. Similarly, when the voltage is greater than 2 V, the temperature of the cell at 5s is higher than 60 °C, which cannot detect defects effectively. Therefore, we chose the bias of 1 V, 1.5 V and 2 V for experiments. The maximum temperature of the cell S1 and S2 and temperature difference between them and a healthy area are presented in Table 1. It is interesting to notice that ΔT remains almost equal in S1 from 1.5 V to 2 V, and ΔT is equal in S2 from 1.5 V to 2 V.

The processing results of thermography sequence of S1 and S2 samples with different bias voltages excitation (1 V, 1.5 V and 2 V) by LDA and QDA are shown in Fig. 9. However, the defect processing results of LDA and QDA under different bias voltages cannot be directly compared from Fig. 9. Therefore, in order to objectively evaluate the performance of the above algorithms for defects recognition under different bias voltages. The SNR of the original thermal images and the images of Fig. 9 is calculated based on formula (16), as shown in Fig. 10.

It can be seen from Fig. 10 that the SNR of the original thermal images of S1 and S2 are significantly improved by LDA and QDA processed. In S1, the SNR value of QDA is the highest under the 1 V. Combined with Fig. 9, it can also be found that the QDA result under 1 V is the most obvious for the identification of hidden crack, scratch and broken gate defects compared to the QDA results at 1.5 V and 2 V. In S2, although the SNR value of QDA is the largest under the 2 V, it is not significant compared to 1 V and 1.5 V. It is also found that the voltage has no obvious effect on the identification effect of hot spot defect in Fig. 9. In summary, the recognition effect of QDA is more obvious, which shows that compared with LDA, defects such as hidden crack, scratch, hot spot and broken gate can be more easily identified by QDA processed.

6. Conclusion

In this paper, EPIT method has been used to detect and analyze the scratch, hidden crack, hot spot and broken gate defects of polysilicon PV cells. LDA and QDA, the two supervised learning algorithms, are used to process the thermography sequence and the SNR performance of LDA and QDA are computed respectively. The experimental results show that EPIT method can detect the defects of PV cells. LDA and QDA select images containing target features in thermography sequence, and use the spectral reflectance vector of target pixels in images, then combine information across the spectral bands by maximizing the output value of spectral vectors similar to a target, and minimizing those resembling background. Finally, the defect recognition is realized. Therefore, LDA and QDA can effectively retain the defect category information. In addition, compared with PCA and LDA, QDA has the best recognition effect for photovoltaic cell defects.

CRediT authorship contribution statement

Runhong Shen: Software.

Declaration of competing interest

The authors declare that they have no known competing financial interests or personal relationships that could have appeared to influence the work reported in this paper.

Acknowledgments

This project is supported by National Natural Science Foundation of China (Grant No. 51775175), Basic Scientific Research Business Expenses of Heilongjiang Provincial Colleges and Universities in 2020 of Heilongjiang University of Science and Technology (Grant No. 2020-KYYWF-0696), Heilongjiang Province Natural Science Fund (Grant No. LH2021E088), and Teacher innovation project in 2021 of Harbin University of Commerce (Grant No. LH2021E088).

References

- [1] B. Du, R. Yang, Y. He, F. Wang, S. Huang, Nondestructive inspection, testing and evaluation for Si-based, thin film and multi-junction solar cells: an overview, *Renew. Sustain. Energy Rev.* 78 (2017) 1117–1151.
- [2] S. Vergura, F. Marino, Quantitative and computer-aided thermography-based diagnostics for PV devices: Part I-Framework, *IEEE J. Photovoltaics* 7 (3) (2017) 822–827.
- [3] B. Du, Y. He, Y. He, C. Zhang, Progress and trends in fault diagnosis for renewable and sustainable energy system based on infrared thermography: a review, *Infrared Phys. Technol.* 109 (2020) 103383.
- [4] C. Schuss, K. Leppänen, K. Remes, J. Saarela, T. Fabritius, B. Eichberger, T. Rahkonen, Detecting defects in photovoltaic cells and panels and evaluating the impact on output performances, *IEEE Trans. Instrum. Meas.* 65 (5) (2016) 1108–1119.
- [5] R. Yang, B. Du, P. Duan, Y. He, H. Wang, Y. He, K. Zhang, Electromagnetic induction heating and image fusion of silicon photovoltaic cell electrothermography and electroluminescence, *IEEE Trans. Ind. Inf.* 16 (7) (2020) 4413–4422.
- [6] M. Abdelhamid, R. Singh, M. Omar, Review of microcrack detection techniques for silicon solar cells, *IEEE J. Photovoltaics* 4 (1) (2013) 514–524.
- [7] X. Li, Q. Yang, Z. Chen, X. Luo, W. Yan, Visible defects detection based on UAV-based inspection in large-scale photovoltaic systems, *IET Renew. Power Gener.* 11 (10) (2017) 1234–1244.
- [8] Y. Wang, L. Li, Y. Sun, J. Xu, Y. Jia, J. Hong, et al., Adaptive automatic solar cell defect detection and classification based on absolute electroluminescence imaging, *Energy* 229 (2021) 120606.
- [9] F. Grimaccia, S. Leva, A. Niccolai, PV plant digital mapping for modules' defects detection by unmanned aerial vehicles, *IET Renew. Power Gener.* 11 (10) (2017) 1221–1228.
- [10] S. Kumar, P. Jena, A. Sinha, R. Gupta, Application of infrared thermography for non-destructive inspection of solar photovoltaic modules, *J. Non Destruct. Test. Eval.* 6 (2017) 25–32.
- [11] Y. He, B. Du, S. Huang, Non-contact Electromagnetic induction excited infrared thermography for photovoltaic cells and modules inspection, *IEEE Trans. Ind. Inf.* (12) (2018) 12–20.
- [12] B. Du, Y. He, J. Duan, Y. Zhang, Intelligent classification of silicon photovoltaic cell defects based on eddy current thermography and convolution neural network, *IEEE Trans. Ind. Inf.* 99 (2019) 1–9.
- [13] F. Fröhlauf, J. Wong, J. Bauer, O. Breitenstein, Finite element simulation of inhomogeneous solar cells based on lock-in thermography and luminescence imaging, *Sol. Energy Mater. Sol. Cells* 162 (2017) 103–113.
- [14] O. Breitenstein, H. Straube, K. Iwig, Lock-in thermography with depth resolution on silicon solar cells, *Sol. Energy Mater. Sol. Cells* 185 (2018) 66–74.
- [15] F. Fröhlauf, O. Breitenstein, DLIT-versus ILIT-based efficiency imaging of solar cells, *Sol. Energy Mater. Sol. Cells* 169 (2017) 195–202.
- [16] O. Breitenstein, J.P. Rakotonaina, Electrothermal simulation of a defect in a solar cell, *J. Appl. Phys.* 97 (7) (2005) 5200–1047.
- [17] J. Gong, Y. Zheng, J. Liu, A study on the SNR performance analysis of laser-generated bidirectional thermal wave radar imaging inspection for hybrid C/GFRP laminate defects, *Infrared Phys. Technol.* 111 (7) (2020) 103526.
- [18] D.G. Manolakis, Taxonomy of detection algorithms for hyperspectral imaging applications, *Opt. Eng.* 44 (6) (2005) 29–43.
- [19] T. Tarumi, G.W. Small, R.J. Combs, R.T. Kroutil, Remote detection of heated ethanol plumes by airborne passive fourier transform infrared spectrometry, *Appl. Spectrosc.* 57 (11) (2003) 1432–1441.
- [20] C. Bu, G. Liu, X. Zhang, Q. Tang, Debonding defects detection of FMLs based on long pulsed infrared thermography technique, *Infrared Phys. Technol.* 104 (2019) 103074.